Journal of Materials Research and Technology 43 (2026) 3150–3163

Contents lists available at ScienceDirect

Journal of Materials Research and Technology

journal homepage: www.elsevier.com/locate/jmrt

Hot isostatic pressing temperature–driven microstructure–tribology relationships in laser powder bed fused pure chromium

Ozkan Gokcekaya [a,b,*], Asli Gunay Bulutsuz [c,**], Buse Gulec [c], Ali Gunen [d], Hakan Yilmazer [e], Takayoshi Nakano [a,b]

[a] Division of Materials and Manufacturing Science, Graduate School of Engineering, The University of Osaka, 2-1, Yamadaoka, Suita, Osaka, 565-0871, Japan
[b] 3DPTec Integrated Center, The University of Osaka, 2-1, Yamadaoka, Suita, Osaka, 565-0871, Japan
[c] Department of Mechanical Engineering, Yildiz Technical University, Besiktas, Istanbul, Turkey
[d] Department of Metallurgy and Materials Engineering, Iskenderun Technical University, 31200, Iskenderun, Hatay, Turkey
[e] Department of Metallurgical and Materials Engineering, Yildiz Technical University, 34220, İstanbul, Turkey

ARTICLE INFO

Keywords:
Refractory metal
Pure chromium
Laser powder bed fusion
Hot isostatic pressing
Microstructure
Wear

ABSTRACT

Conventional processing of chromium has long been abandoned due to its high ductile-to-brittle transition temperature (DBTT), which promotes stress-induced cracking during solidification. Nevertheless, chromium and its alloys remain attractive for advanced applications because of their excellent high-temperature stability, oxidation resistance, and tribological performance. In this study, pure chromium was fabricated by laser powder bed fusion (LPBF) using optimized processing parameters, followed by hot isostatic pressing (HIP) at moderate and high temperatures to address LPBF-induced cracking and residual stresses. The influence of HIP temperature on microstructural evolution, mechanical properties, and tribological behavior was systematically investigated. HIP effectively improved densification and reduced internal defects; however, the HIP temperature strongly governed the balance between residual stress relief and grain growth. As-built LPBF chromium exhibited high hardness and wear resistance due to its fine grain structure and retained residual stresses. HIP at a moderate temperature was sufficient to relieve residual stress while preserving the fine microstructure, thereby maintaining favorable mechanical and tribological performance. In contrast, high-temperature HIP promoted pronounced <100> grain growth, which facilitated the formation of a stable oxide layer and enhanced lubricating effects during sliding, but at the expense of mechanical strength due to excessive grain coarsening. These results highlight the critical role of HIP temperature in tailoring microstructure–property relationships in additively manufactured pure chromium while suggesting implementation of strategies to suppress grain growth while leveraging the combined benefits of LPBF and HIP processing for refractory metals.

1. Introduction

Refractory metals and alloys have been the subject of extensive research for many years due to their exceptional material performance under extreme conditions [1–3]. Chromium (Cr), in particular, stands out among materials used in high-temperature and corrosive environments, owing to its excellent oxidation and corrosion resistance and high melting point [3–5]. For instance, pure Cr is commonly employed as a coating material in optical and electronic devices to enhance corrosion and wear resistance [6]. Its remarkable ability to maintain corrosion and wear resistance even at elevated temperatures makes body-centered cubic (BCC) Cr an attractive material for high-temperature applications [3,7]. However, despite these advantages, pure Cr's mechanical weaknesses, such as low toughness and brittleness due to its high DBTT, present significant challenges for conventional manufacturing methods. Its high melting point (T_m, 1907°C) further complicates traditional production, making these processes costly and complex, thus limiting the broader industrial application of Cr [8–10].

Recent advancements in additive manufacturing (AM) have provided innovative solutions to many of these challenges, particularly in

---

* Corresponding author. Division of Materials and Manufacturing Science, Graduate School of Engineering, The University of Osaka, 2-1, Yamadaoka, Suita, Osaka, 565-0871, Japan.

** Corresponding author.

E-mail addresses: ozkan@mat.eng.osaka-u.ac.jp (O. Gokcekaya), gunay@yildiz.edu.tr (A.G. Bulutsuz).

https://doi.org/10.1016/j.jmrt.2026.06.191
Received 5 February 2026; Received in revised form 18 June 2026; Accepted 20 June 2026
Available online 22 June 2026
2238-7854/© 2026 The Authors. Published by Elsevier B.V. This is an open access article under the CC BY license (http://creativecommons.org/licenses/by/4.0/).

processing materials like hard-to-process Cr [11] due to its high melting temperatures and brittle nature. AM techniques offer numerous advantages, including process parameter control to optimize solidification and microstructure, besides their ability to produce complex geometries and the rapid manufacturing of customized parts [12]. These benefits have expanded the use of Cr in industries requiring high-temperature and corrosion resistance, such as aerospace, energy, and automotive sectors. In particular, Cr components produced via AM can endure service temperatures up to 1000°C, making them ideal for high-performance applications like turbines and engine components [9].

Among the various AM techniques, Laser Powder Bed Fusion (LPBF) has gained prominence for producing high-quality, dense metal parts from metal powders. However, challenges such as residual stress and surface quality issues remain, particularly for metals with high melting points like Cr alloys [13,14]. LPBF typically utilizes spherical powder produced through gas atomization for the powder flowability concern. However, this practice is associated with increased time and cost for AM processes, therefore, the study on refractory Cr was utilized with a cost-efficient powder production resulting in irregular shape. Although the LPBF process parameters were optimized for the irregular powder, post-processing, such as hot isostatic pressing (HIP), is commonly employed to address the limitations regarding defects induced by refractory nature of Cr. HIP is widely used to reduce porosity and enhance the mechanical properties of AM parts, making them suitable for critical applications in sectors like aerospace and medical industries [15,16].

The continued evolution of AM technologies, combined with processes like HIP, is driving the broader adoption of Cr and its alloys in industrial applications. This shift is revolutionizing traditional manufacturing by offering cost-effective, flexible, and efficient solutions for producing high-performance materials that meet stringent industry standards [17,18]. Studies have shown that samples subjected to HIP exhibit higher mechanical properties compared to those without HIP treatment. After applying HIP to Fe–Cr–Ni alloys, a ~6% increase in tensile strength and a ~10% improvement in room temperature elongation were observed [19]. In studies focusing on the HIP process, the influence of temperature has been specifically examined, with material porosity and mechanical properties analyzed at various temperature levels to determine the optimal HIP temperature [20,21]. In Cr-containing alloys, the application of HIP reduces porosities and manufacturing-induced voids, improves grain structure, and enhances tensile strength. Furthermore, research on other alloys has demonstrated that reducing the porosity in additively manufactured parts increases density and improves mechanical properties [20–22]. As a result, the part becomes more reliable in terms of strength, making it more suitable for use in applications requiring high strength.

While the HIP post-processing is expected to reduce the defects (pores, lack of fusion, and cracks), the HIP temperature plays a critical role in terms of final microstructural features of AMed metals and alloys, such as density, grain size, texture, dislocation density, phase formation/fraction, and so on [23]. Thus, determination of HIP temperature is important for mechanical performance considering its high melting point. As cubic lattice systems (BCC and FCC) prefer <100> texture development along the build direction during LPBF process, Cr and 316L stainless steel developed <100> texture by LPBF process with optimized process parameters. The enhanced oxidation behavior of LPBFed Cr with <100> texture has been reported [11]. Moreover, tribological studies on textured 316L stainless steel indicated that grain orientation section during epitaxial growth and formation grain boundaries should be considered for wear performance regarding the effect of applied shear stress on the surface and the formation of lubricating tribo-film [24]. While Aghayar et al. reported enhanced mechanical properties and corrosion resistance of LPBFed 316L after HIP post-processing owing to homogeneity in microstructural features and decrease in defects [25,26]. These reference studies highlight the impact of microstructural features on mechanical performance not only in terms of hardness but also tensile, fatigue, electro-corrosion, and tribo-corrosion in aspect of dislocation motion and formation of lubricating film, such as protective oxide film.

In the literature, various combinations of LPBF and HIP process parameters were selected to deliberately manipulate the final microstructure to achieve additively manufactured products with reduced defects for structural applications [27,28]. This study was prompted by the growing need in literature for a comprehensive exploration of the effects of HIP temperature on cracks, microstructural features, and tribological properties of additively manufactured pure Cr to guide the research focusing on refractory metals and alloys processed by LPBF.

2. Materials and methods

2.1. LPBF processing of pure Cr

Irregularly shaped pure Cr powder with a purity greater than 99% (JFE Material, Japan) was used to manufacture 5 × 5 × 5 mm cube samples via LPBF, as illustrated in Fig. 1a. It is important to note that the Cr powder was produced using a cost-effective method, resulting in irregular particle shapes, however, its particle size distribution (*Dx(50)* = 44.8 μm) and flow properties—such as an avalanche angle of 52.8° and a surface fractal of 1.95—were adequate for the LPBF process [29], as shown in Fig. 1.

The pure Cr samples were fabricated on a 316L stainless steel base plate using an EOS M290 LPBF machine (Germany), equipped with a 400W Yb laser with a beam diameter of 100 μm. Additionally, the build platform was preheated to 200°C. The LPBF process parameters, previously optimized in an earlier study [11,29], were applied as follows: a layer thickness (h) of 20 μm, laser power (P) of 300 W, scanning speed (V) of 800 mm/s, and hatch spacing (d) of 80 μm (Table 1). The volume energy density (E) for the LPBF process can be calculated using Eq. (1), which is equal to 234.4 J/mm^3.

$$E = \frac{P}{V \times h \times d} \tag{1}$$

2.2. Hot isostatic pressing

The HIP parameters were set at 100 MPa and two different temperatures, 1250°C (T/T_m (K) > 0.5) and 1500°C (T/T_m (K) > 0.8), to examine the influence of temperature under optimized HIP pressure as our previous study stated that low HIP pressure can improve densification while high HIP pressure exhibited a negative effect on the density of Cr components processed by LPBF [27]. Therefore, the effect of the HIP temperature on defects of LPBF-processed Cr was of interest in this study using a non-destructive Archimedes' principle in accordance with the ASTM B962 Standard. A precision lab balance equipped with a density measurement device for solid materials was used to measure density in alcohol at room temperature, with an accuracy of 0.001 g. This approach does not account for central defects. Image processing techniques were applied to optical microscope images to investigate the defects in the top, center, and side regions.

2.3. Microstructural characterization

Optical microscopy (OM) images were taken parallel (xy plane) and perpendicular (yz plane) to the LPBF build direction to investigate the characteristics of defects, as illustrated in Fig. 1. To prepare the sample surfaces, they were initially polished with sandpaper of 320–2500 grit. This was followed by fine polishing using a 1 μm polishing cloth and a 0.01 μm alumina solution. Afterwards, the samples were cleaned by immersing them in ethyl alcohol and placing them in an ultrasonic cleaner before microscopy observations.

OM was employed to assess the defect percentages and analyze the microstructure. The obtained OM images were processed with ImageJ software to calculate each sample's density by measuring the cross-

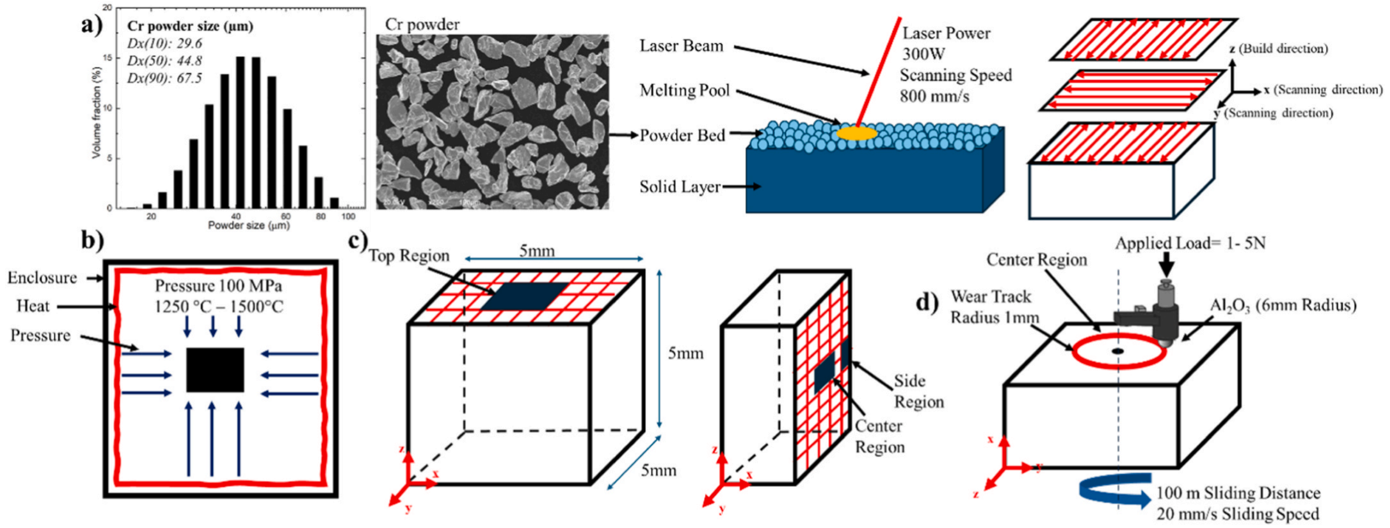

Fig. 1. a) Irregular Cr powder's image and its size distribution with illustration of applied LPBF process parameters and scan strategy, b) HIP process details, and c) porosity measurement regions with the illustration of d) wear test details.

Table 1
Processes parameters of LPBF and HIP methods.

Samples	Laser power (W)	Scan speed (mm/s)	HIP temperature (°C)	HIP pressure (MPa)
As-built Cr	300	800	–	–
Cr-1250	300	800	1250	100
Cr-1500	300	800	1500	100

section's defect area ratio. The defects, including cracks, lack of fusion, and porosity, were quantified as a percentage of the total analyzed area. Each sample's surface measurements were repeated five times, after which the average values and standard deviations were calculated.

The microstructure of both the as-built and HIP-treated Cr samples was investigated using an electron backscatter diffraction (EBSD) system (Nordlys Max3 system, Oxford Instruments, Cambridge, UK) integrated with a field-emission scanning electron microscope (FE-SEM; JIB-4610 F, JEOL, Tokyo, Japan) operated at an accelerating voltage of 20 kV and with a 2 μm step size. Data collected from these investigations were analyzed using HKL Channel5 software (Oxford Instruments, UK) to generate inverse pole figure (IPF) maps, pole figures, grain size distributions, and qualitative and quantitative assessments of grain boundaries (GBs), Kernel average misorientation (KAM), and grain characteristic distributions.

2.4. Hardness and tribological characterizations

The hardness of the samples was determined using a Vickers Hardness Tester. Five separate measurements were taken from different regions of the surface of each sample, using a 500 gf load for 15 s. The mean values and standard deviations were calculated through statistical analysis.

For the wear tests, a radial motion was performed against a ceramic ball as the counterface material using a Tribotester (Tribo Technic). The ceramic ball used in the tests, made of Al_2O_3 with a 6 mm diameter, had a Vickers hardness of 1800 Hv and served as the abrasive. A normal load (1 N and 5 N) was applied at a rotational speed of 20 mm/s under dry conditions. The tests were done on the polished center region, as shown in Fig. 1d. The wear track radius was 1 mm for a test length of 100 m. The ceramic balls were secured following ASTM G99–05 standards. The coefficient of friction (CoF) values were obtained from the friction force data recorded during the wear tests. Each wear test was repeated three times for each condition. The mean CoF values were calculated based on stabilized regions of the frictional force graph after 40 m of sliding distance, which excludes the running-in stage.

The surface topographies and wear track width were observed through investigations using a field-emission scanning electron microscope (FE-SEM, Thermo Scientific). FE-SEM Energy Dispersive Spectroscopy (EDS) mapping was conducted to determine the wear mechanisms. Ten repetitive measurements of the wear track width were performed to calculate the average value. Wear volume loss was calculated using Eq. (2) according to the ASTM G99-17:

$$Volume\ loss = 2\pi R\left[r^2 \sin^{-1}\left(\frac{d}{2r}\right) - \left(\frac{d}{4}\right)\left(4r^2 - d^2\right)^{\frac{1}{2}}\right] \tag{2}$$

where: R = wear track radius, r = abrasive ball radius, d = wear track width, assuming no significant pin wear.

In addition, the wear track widths, volumes, and surface topographies were analyzed using 3D optical profilometry. A Polytec TopMap Micro View device with a 10× objective lens was used for the measurements. Each wear track was measured three times to ensure accuracy. The entire wear scar was considered when calculating the volume.

3. Results

3.1. Porosity

The OM images and corresponding quantitative data highlight the effects of LPBF process and HIP post-process treatment at 1250°C and 1500°C on the crack density of Cr samples. The OM images for crack measurements were taken from top (xy plane), center, and side regions (yz plane) as shown in Fig. 2 and quantitatively summarized in Table 2. The as-built sample exhibits significant cracking on the top surface along grain boundaries, distinctive to the XY scan strategy [30], and lack of fusion due to insufficient melting or unstable melt pool formation was detected at the center and side regions. The major defect characteristics was crack formation along GBs due to residual stress caused by rapid cooling during the LPBF process. The top region showed higher ratio of cracks due to residual stress and higher rate of HAGBs than the center and side regions where epitaxial growth was expected to form columnar grain owing to layer-by-layer melting. With reconsideration of process parameter setting up higher laser power (300W) and scan speed (800 mm/s) with the same VED compared to our previous study (150W–400 mm/s) [27], the porosity in the center and side regions was

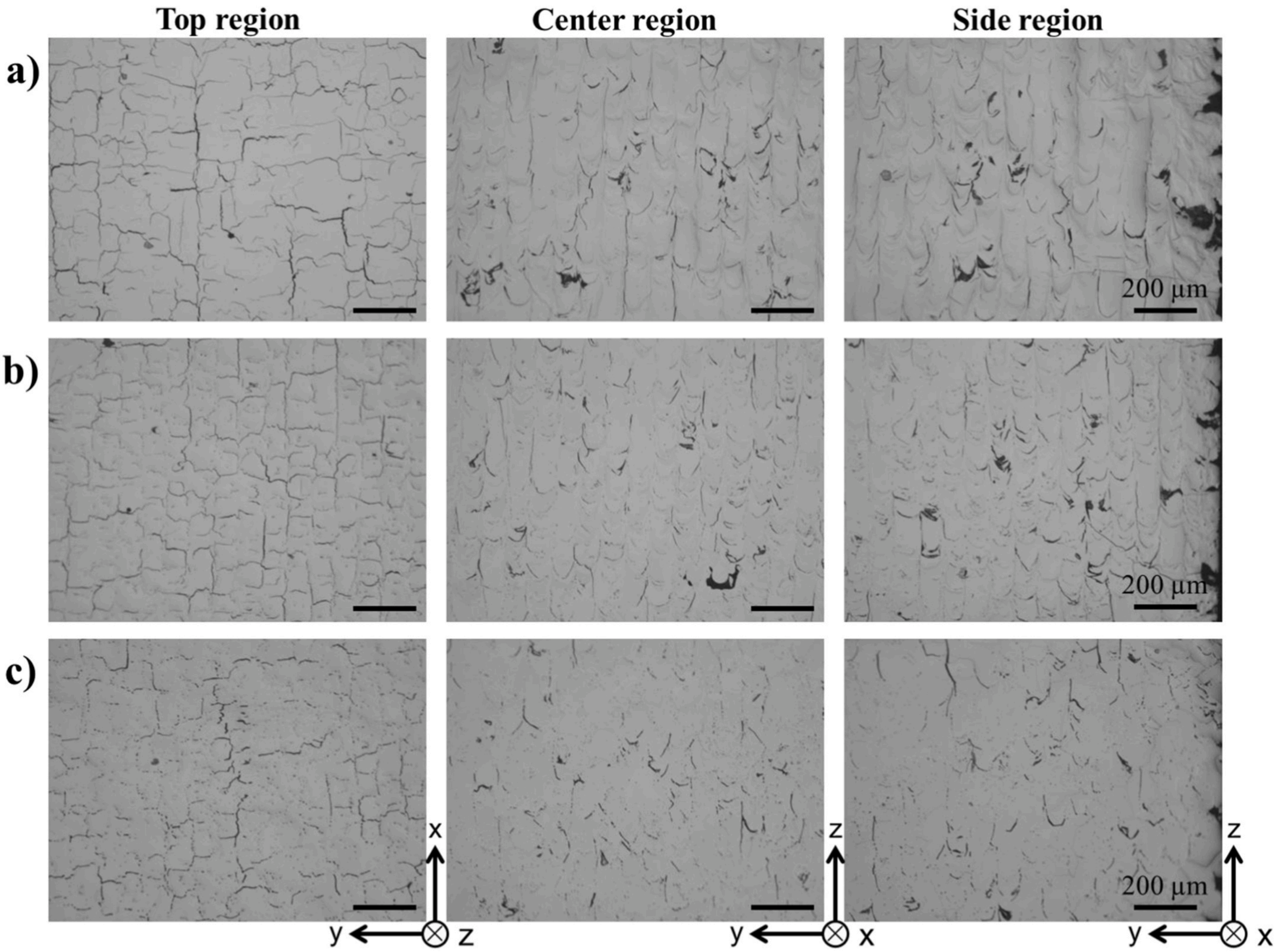

Fig. 2. OM images taken from top, center, and side regions of a) as-built Cr sample, b) HIPed Cr-1250 sample, and c) HIPed Cr-1500 sample.

Table 2
Percentage of cracks in as-built and HIPed Cr samples.

Samples	Cracks		
	Top region (%)	Center region (%)	Side region (%)
As-built Cr	5.70 ± 0.34	4.45 ± 0.90	4.30 ± 0.86
Cr-1250	7.28 ± 0.13	4.39 ± 0.34	4.51 ± 0.26
Cr-1500	4.90 ± 0.35	3.75 ± 0.18	3.81 ± 0.33

homogenized for consistent structural performance. The center region exhibits fine microcracks and some residual pores from incomplete diffusion, resulting in 4.45% porosity, while the side region has slightly lower porosity with fewer cracks but more lack of fusion defects, as shown in Fig. 2a, which might relate to the difference in cooling rate of center and edge of the component processed by LPBF.

While the HIP-1250°C sample showed improvements in microstructural homogeneity in terms of cracking with smaller deviation, crack ratio increased in the top and side regions. This suggests that the HIP process at 1250°C was insufficient to completely eliminate cracks, particularly the ones open to the surface. Furthermore, although some cracks were noted to have closed in the top region, the overall defect density in the side and top regions was increased due to the propagation of open-surface cracks under pressure. This highlights that while HIP treatment can be effective in certain areas, it may not be capable of eliminating all defects uniformly throughout the sample and could, in some cases, lead to the growth of existing defects, particularly open-surface ones [31].

The HIP-1500°C sample (Fig. 2c) shows crack healing tendency and better structural integrity at the top, center, and side regions, where crack ratio remains lower than in the other samples, 4.90%, 3.75%, and 3.81%, respectively. However, the highest porosity (4.90%) of this sample was measured at the top region, similar to other conditions, due to higher initial porosity and open-surface characteristics of cracks. While the HIP temperature and pressure resulted in closure of some cracks in each region, the center region showed the lowest crack density for Cr-1500, although complete elimination of defects was not realized.

The density of Cr samples determined by Archimedes' principle is given in Table 3, demonstrating the effect of HIP temperature compared to as-built Cr. The as-built sample exhibited a density of 6.77 ± 0.49 g/cm^3, reflecting the intrinsic defects commonly associated with the rapid solidification and layer-by-layer nature of the LPBF process, forming

Table 3
Density, hardness, and high-angle grain boundary (HAGB) density values of as-built and HIPed Cr samples.

Samples	Density (g/cm^3)	Hardness (Hv)	HAGB density (%)	Grain size (µm)
As-built Cr	6.77 ± 0.49	183.55 ± 8.45	41.2	19.0
Cr-1250	6.50 ± 0.17	156.01 ± 10.69	35.1	22.3
Cr-1500	7.03 ± 0.07	125.50 ± 6.91	14.3	50.3

cracks along HAGBs. After HIP treatment at 1250°C, the density decreased slightly to 6.50 ± 0.17 g/cm^3, which can be attributed to the thermal relaxation of residual stresses, potentially allowing the redistribution of pores and cracks. However, with HIP at 1500°C, the density significantly increased to 7.03 ± 0.07 g/cm^3, approaching the theoretical density of pure Cr (7.19 g/cm^3, [11]). This increase points to the closure of internal defects/cracks and increased structural integrity.

The correlation between Archimedes' density measurement and optical defect measurements can be realized with the top and side values, as expected, since the Archimedes measurement does not consider internal porosity. On one hand, the top and side regions of HIP at 1250°C exhibited increase in percentage of defects (Table 2) the Archimedes measurements presented decrease in density value. On the other hand, the tendency of crack percentage and density measurements for HIP at 1500°C were reversed, showing decrease in cracks and increase in density. Therefore, the tendency in density measurement with the top and side region porosity showed corresponding values. Moreover, the future implementation of such brittle refractory metals and alloys for component production via AM processes requires surface finish, such as machining, thus it is expected to remove the high defect region for the final component. Besides, the center region demonstrated crack closure with the HIP process, as identified with OM measurements, and HIP-1500°C reached the lowest defect level and highest component density, indicating the effect of HIP temperature on crack healing behavior. While increased density owing to crack closure was expected to improve bulk mechanical performance, the densification with HIP processing, particularly HIP at 1500°C, did not correlate with the hardness values; instead, hardness values were determined by the grain size and high-angle grain boundary (HAGB) density (Table 3). The increase in grain size and consequent decrease in HAGB density caused a decrease in the hardness of HIPed Cr samples. This suggests that HIP parameters, particularly temperature, need to be carefully optimized to balance bulk and surface characteristics.

3.2. *Microstructure characteristics*

Microstructure analyses of as-built Cr processed by LPBF and subsequently densified by HIP process at 1250°C and 1500°C with under 100 MPa pressure were carried out, focusing on grain orientation, HAGB distribution, grain size, residual stress (identified by KAM), and grain characteristics parallel to the build direction, corresponding to the wear test surface. The results presented the significant effect of HIP processing temperature on microstructural features of as-built Cr. The effect of temperature on microstructural features was significant. Although the HIP process at 1250°C (T/T_m (K) > 0.5) wasn't high enough to promote recrystallization but sufficient to reduce the stress [27], it was ineffective to promote significant grain growth to reduce HAGBs, which are crack initiation and propagation sites under mechanical load. Therefore, high HIP temperature, 1500°C (T/T_m (K) > 0.8), was investigated to determine the crack-healing via grain growth [32] while pre-softening before the HIP process also exhibited promising results [33] to eliminate solidification cracks.

The microstructural features of as-built and HIPed Cr were assessed by EBSD measurements, as shown in Fig. 3, which presented the grain orientation distribution with IPF maps and {100} pole figures, besides HAGB maps demonstrating the grain boundary structure, which is important to understand the mechanical performance of the samples. The grain orientation of as-built and Cr-1250 showed similar characteristics with the distribution of mainly <100> and <110> oriented grains, indicating HIPed at 1250°C had no significant effect on grain

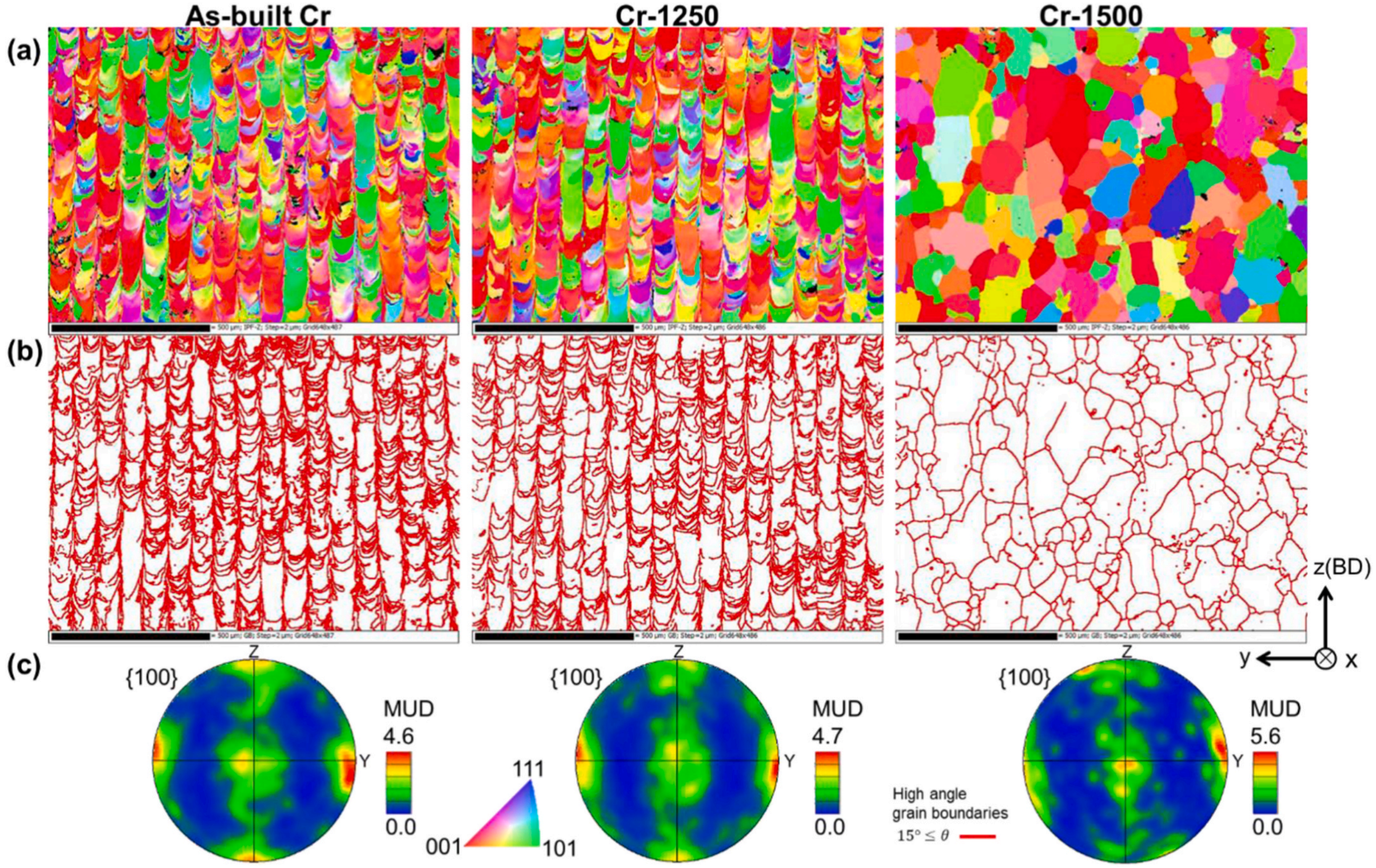

Fig. 3. Microstructural features of as-built Cr, HIPed Cr-1250 and Cr-1500 samples; grain orientations and structure represented with (a) inverse pole figure (IPF) and (b) high-angle grain boundary (HAGB) maps, respectively, with (c) corresponding {001} pole figures. Scale bars indicate 200 μm.

orientation distribution. Although the crystallographic texture was comparable after the HIP process at 1250°C to as-built Cr, the HAGB distribution of Cr-1250 exhibited a decrease in density (Table 3), implying the occurrence of slight grain growth at this HIP condition. Fig. 4, showing the average grain size and its distribution, supports this finding, exhibiting a higher fraction of bigger grains with an increase in grain size from 19 μm to 22.3 μm.

However, the grain characteristics exhibited significant differences after performing HIP at 1500°C to as-built Cr samples. While grain growth was evidently observed from the IPF map of Cr-1500 (Fig. 3), the consequent decrease in HAGB density and increase in grain size (Table 3) demonstrated the significant effect of the HIP process at 1500°C on microstructure characteristics of as-built Cr. In this context, Cr-1500 samples displayed high-rate recrystallization, resulting in grain growth, reaching over 2.5 times of the as-built Cr grain size (from 19 μm to 50.3 μm). The grain structure of Cr-1500 was equiaxed after recrystallization with an increase in multiple uniform distribution (MUD) to 5.6, indicating that the {100} easy growth direction of BCC Cr was preferred for recrystallization and grain growth, achieving microstructural isotropy. These findings on microstructure characteristics comparing as-built Cr to HIPed ones processed at 1250°C and 1500°C demonstrated the importance of the HIP temperature regarding recrystallization and grain orientation. Therefore, the difference in mechanical strength and tribological performance of as-built and HIPed Cr was expected, considering the effect of grain orientation on oxidation behavior and grain size on the hardness of the samples.

Moreover, the HIP process did not only affect the grain orientation and size but also altered the residual stress of the as-built Cr depending on the applied temperature. The KAM maps, representing residual stress distribution as an indication of dislocation characteristics, presented in Fig. 5 elucidated the decreasing tendency of stress with HIP application. The highest residual stress value (identified by KAM, θ = 0.94°) was detected for as-built Cr due to the fast cooling and cycling heating during LPBF process, resulting in extreme residual stress by the repetitive melting and solidification process. However, the HIP process showed temperature-dependent stress relief as observed on KAM maps and quantitative KAM distribution. Therefore, Cr-1250 showed a 23% (θ = 0.72°) decrease in KAM value. More importantly, an increase in HIP temperature to 1500°C (Cr-1500) demonstrated a 77% (θ = 0.22°) decrease in average KAM value. Besides, the decreasing tendency in KAM was evident in KAM maps, as shown in Fig. 5, clarifying the significant effect of HIP temperature on residual stress as an important microstructural feature to explain the hardness and wear properties of Cr.

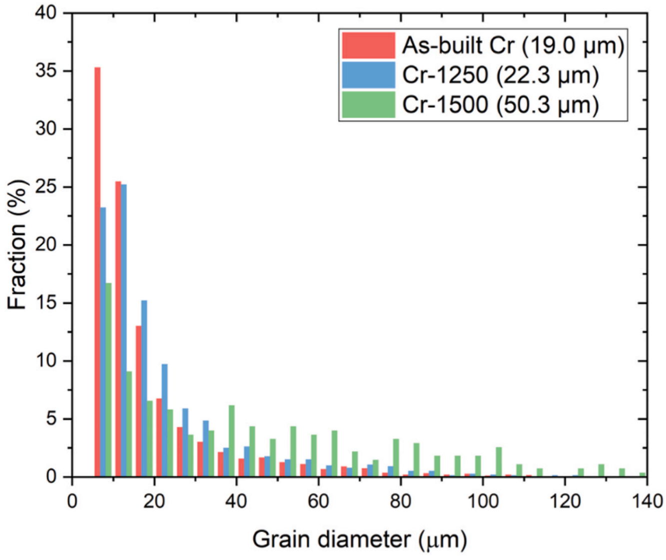

Fig. 4. Grain size distribution and average grain size of as-built and HIPed Cr samples (data driven from the measurements presented in Fig. 2).

The differences in residual stress after LPBF and HIP processes were expected to alter the grain characteristics, while LPBF produces high residual stress due to the fast-cooling rate but the HIP process tempers the stress depending on the applied temperature and tuned the grain characteristics as shown in Fig. 6. As expected, as-built Cr showed a high ratio of deformed grains reaching over 70%. However, HIP at 1250°C exhibited partial recovery with accompanying decrease in residual stress (Fig. 5), thus decreasing the deformed grain rate to 48% and increasing the substructure grain ratio to 47% (Cr-1250, Fig. 6), thus resulting in a slight increase in grain size (Fig. 4) while likely promoting subgrain boundaries [34].

Moreover, HIP at 1500°C exhibited near-full recovery of the deformed grains and increased the recrystallized grain ratio to 90% with only about 1% remaining deformed grain owing to the application of such high temperature, T/T_m(K) reaching over 0.8. Thus, Cr-1500 exhibited grain growth and a decrease in stress. This indicates that the HIP process can be implemented not only to densify the components but also to tune the grain characteristics with the applied temperature to mitigate anisotropy.

3.3. *Tribological properties*

The as-built sample exhibited the highest hardness, 183.55 ± 8.45 HV, attributed to its finer microstructure and inherent residual stresses from the LPBF process (Table 3). However, post-HIP processing decreased hardness due to grain growth and relaxation of internal stresses. The sample processed at 1250°C retained moderate hardness, 156.01 ± 10.69 HV, balancing structural densification and grain coarsening. In contrast, the sample processed at 1500°C showed the lowest hardness, 125.50 ± 6.91 HV, due to excessive grain growth.

The CoF values were measured under 1 N and 5 N loading conditions, and the results are given in Table 4 and Fig. 7. For the 1 N loading test condition, the as-built sample resulted in the highest CoF (0.87 ± 0.03), which means an increase in the frictional resistance. On the other hand, after the HIP process, samples showed reduced CoF values (0.81 ± 0.02 at 1250°C and 0.84 ± 0.03 at 1500°C) with the changes in the surface's properties like oxide amount, pore redistribution, surface cracks, partial densification, and microstructure characteristics. Especially the higher CoF of the Cr-1500 sample may be linked to the increased grain size and reduced stress, as the sample was mechanically weakened after exposure to high temperature. According to these results, while the HIP process reduces internal defects, higher temperatures can decrease mechanical strength due to grain coarsening. On the other hand, higher temperature HIP enabled a delayed increase in CoF during the initial stages of sliding under 1 N loading conditions (Fig. 7a). This behavior points to a more continuous oxide layer in the surface and improved resistance to wear related surface damage.

Under a 5 N loading condition, CoF values decreased for all samples with surface flattening and increased material accommodation under higher load. The as-built sample had a CoF of (0.72 ± 0.05), while the HIP-processed samples demonstrated further reductions to (0.71 ± 0.03 at 1250°C and 0.68 ± 0.01 at 1500°C) (Table 4). The Cr-1500 sample exhibited the lowest CoF, indicating the dominance of bulk densification over surface porosity effects in reducing friction at higher loads. A slight delay in the CoF graph during the initial cycles was observed for the Cr-1500 sample. Parallel to the 1 N loading condition this behavior was attributed to the improved oxide layer continuity which slightly delayed plastic deformation (Fig. 7 (b)).

In Figs. 8 and 9 and Table 4, the wear track information obtained from SEM and 3D optical microscope is given. After 1 N load tribological tests, the narrowest wear track width was observed for the as-built sample (247.30 ± 14.87 μm) and consequently lowest wear volume. The higher hardness (183.55 ± 8.45 HV) of the sample supports this lower wear track width. The wear volume for the as-built sample was

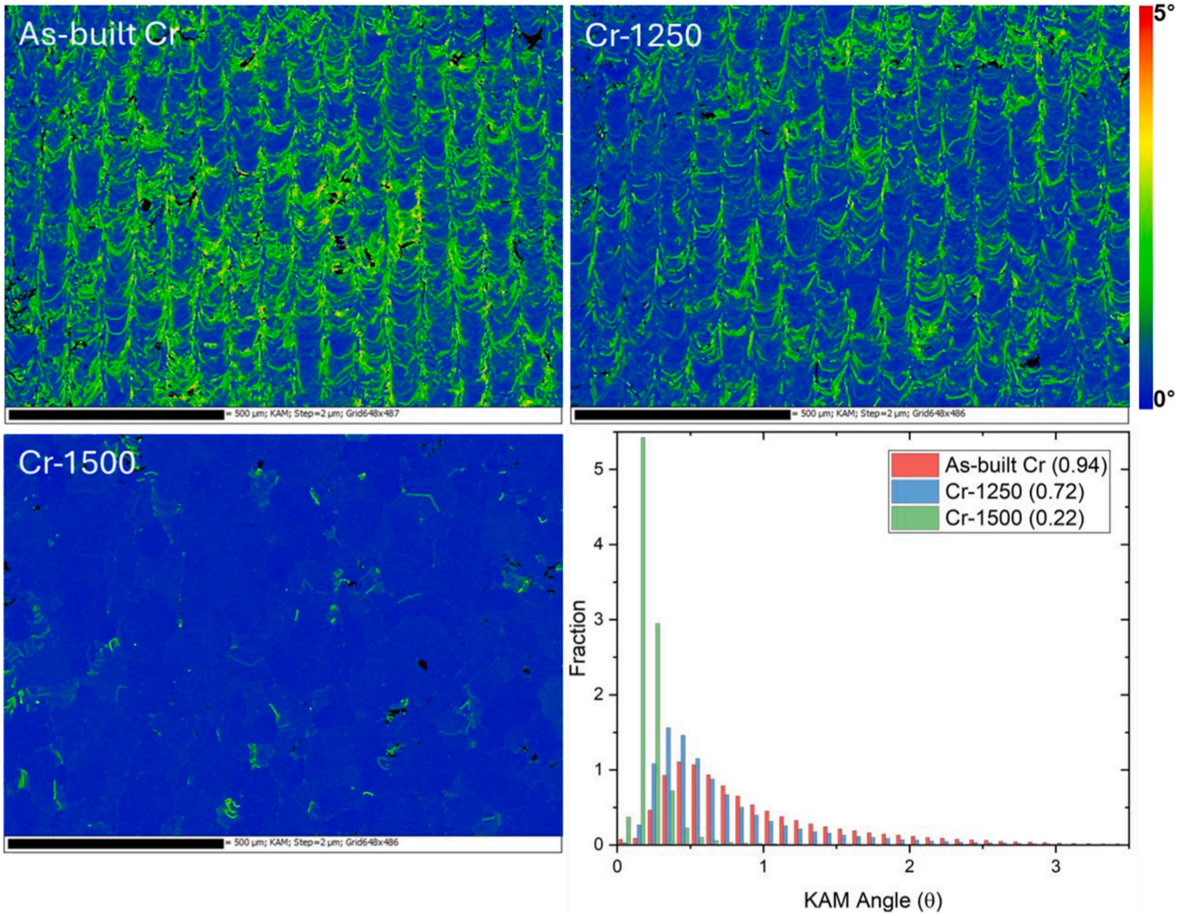

Fig. 5. Kernel Average Misorientation (KAM) maps and the angle distributions of as-built Cr, HIPed Cr 1250, and HIPed Cr 1500 samples. Corresponding to the measurement in Fig. 2.

$0.26 \pm 0.06 \times 10^2$ mm^3. The wear track widths increased after HIP processing to 321.83 ± 21.59 µm at 1250°C and 369.11 ± 11.64 µm at 1500°C. This behaviour is attributed to the softening of the material due to grain coarsening and reduced residual stress. The wear volumes of these samples were measured as $0.58 \pm 0.04 \times 10^2$ mm^3 for the 1250°C sample and $0.87 \pm 0.07 \times 10^2$ mm^3 for the 1500°C sample.

Under a 5 N loading condition, the wear track widths increased for all conditions, which measured as 455.65 ± 17.95 µm for the as-built state and the HIP-processed samples at 492.14 ± 49.60 µm (1250°C) and 902.78 ± 14.71 µm (1500°C), highlighting the reduced wear resistance at higher HIP temperatures. The measured wear volume for the as-built sample was $1.65 \pm 0.12 \times 10^2$ mm^3. For the HIP-processed samples, the wear volumes were $2.08 \pm 0.37 \times 10^2$ mm^3 and $7.21 \pm 0.49 \times 10^2$ mm^3 for 1250°C and 1500°C, respectively.

EDS mapping of the as-built sample under 1 N and 5 N loads revealed the distribution of Cr (chromium), C (carbon), and O (oxygen) along the wear track. This result points adhesive and abrasive wear mechanism and oxidised wear debris. The possible surface contamination from tribo film formation was observed as C element. Materials transfer from the Al_2O_3 abrasive was not detectable in the EDS analyses for either loading conditions (Figs. 8 and 9). This observation supports that, especially under the 5 N load, surface deformation and oxidation of the Cr sample led to material removal and debris formation, contributing to a three-body abrasive–adhesive wear mechanism rather than direct material transfer from the Al_2O_3 counterface.

Figs. 10–11 presents 3D profilometric views of the wear tracks for the as-built and HIP-treated samples under 1 N and 5 N loads. According to the profilometric analysis, for the as-built Cr under 1 N loading condition the narrowest and shallowest wear track with debris accumulation at the edges was observed. This result was consistent with the smallest track width (247.30 ± 14.87 µm) and the lowest wear volume among the three conditions as given in Table 4 and Figss. 10–11.

After HIP treatment, both width and depth increased (Fig. 11b–c). As seen in Fig. 11b, for the 1250°C sample, mild ridges of adhered material are visible along the track edges, and intragroove wear debris accumulation was observed (Fig. 11), indicating that material was removed via ploughing. The broadest track and a noticeably deeper wear pit were visible for the HIP-1500°C sample (Fig. 11c). Substantial material pile-up at the edges were observed, and wear debris appears more prevalent on this surface (Fig. 11c). These results were parallel to the quantitative data in Table 4, which showed increasing wear track width (from 321.83 ± 21.59 µm to 369.11 ± 11.64 µm) and volume loss with higher HIP temperatures. The data also corroborates the SEM observations in Fig. 8.

For the 5 N loading (Fig. 11d–f) condition, all samples display broader and deeper wear tracks compared to 1 N condition, accompanied by more pronounced edge deformation from plastic wear. For the as-built sample (Fig. 11d), considerably wider tracks were observed than 1 N loading condition, with clear material uplift along the track edges and some wear debris smeared within the track. Still, the wear scar remained smaller relative to the HIP-treated samples, reflecting the as-built microstructure's higher hardness and better wear resistance at this load. For the HIP-1250°C sample (Fig. 11e) a further increase was observed in track width and depth relative to the as-built condition. The wear groove in Fig. 11e was slightly wider, in agreement with its 492.14 ± 49.60 µm track width, and deeper, with noticeable edge flow and particle debris accumulation, indicating a moderate degree of material removal. The highest wear was observed for the HIP-1500°C sample at 5

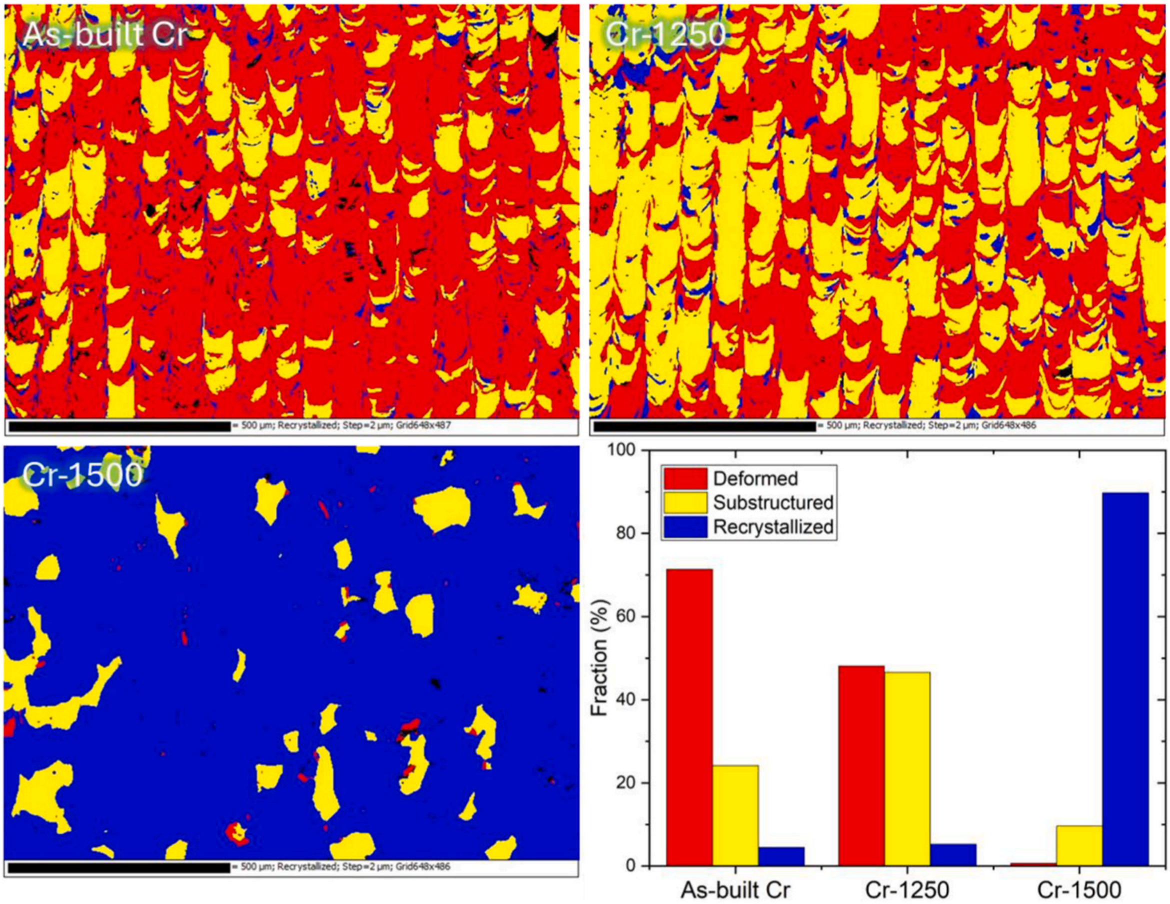

Fig. 6. Recrystallization maps of as-built Cr, HIPed Cr-1250 and Cr-1500 samples with the quantitative analysis of grain characteristics. Corresponding the measurement in Fig. 2.

Table 4
Wear results of as-built and HIPed Cr samples under the 1 N and 5 N loading conditions.

Samples	Coefficient of Friction 1 N	Coefficient of Friction 5 N	Wear Track Width (μm) 1 N	Wear Track Width (μm) 5 N	Wear Track Volume (mm^{3}x10^2) 1 N	Wear Track Volume (mm^{3}x10^2) 5 N
As-built Cr	0.87 ± 0.03	0.72 ± 0.05	247.30 ± 14.87	455.65 ± 17.95	0.26 ± 0.06	1.65 ± 0.12
Cr-1250	0.81 ± 0.02	0.71 ± 0.03	321.83 ± 21.59	492.14 ± 49.60	0.58 ± 0.04	2.08 ± 0.37
Cr-1500	0.84 ± 0.03	0.68 ± 0.01	369.11 ± 11.64	902.78 ± 14.71	0.87 ± 0.07	7.21 ± 0.49

N (Fig. 11f), which presents an exceptionally broad and deep wear track. The profilometry revealed a large gouge with widespread edge deformation and a high degree of particle accumulation, which are detached particles. This corresponds to the increase in wear metrics for the 1500°C–HIP sample relative to the as-built sample (Table 4). Such extensive damage is indicative of an intense abrasive–adhesive wear mechanism under high load. Indeed, the SEM image of the 5 N wear track for this sample (Fig. 9c) showed much wider grooves and severe surface disruption, pointing to dominant plastic deformation and three-body abrasive wear in the Cr-1500 condition.

4. Discussion

4.1. The effect of HIP temperature on microstructural features

Pure Cr has been a critical alloying element to enhance the mechanical properties of many alloy systems. However, the utilization of pure Cr was limited due to its high DBTT, causing HAGBs to be prone to cracking during solidification. This phenomenon is the major reason for the difficulty in densifying pure Cr fabricated by LPBF, which has a high cooling rate causing residual stress, thus limiting its structural applications. This study demonstrated that LPBF-processed pure Cr having cracks that differed in density at the top, center, and side regions due to the difference in cooling rates and remelting during layer-by-layer process [35]. Moreover, our previous study stated that HIP processing can improve the density at low-pressure applications, while high HIP pressure exhibited a negative effect on the density of Cr components processed by LPBF [27]. Our previous findings raised the question of the effect of HIP temperature on the microstructure and tribological performance of as-built Cr with the application of optimum HIP pressure (100 MPa), which was the focus of this study.

The as-built Cr exhibited cubic-like <100> texture development owing to the epitaxial growth along the preferred <100> easy growth axis. It is important to note that the <100> textured Cr surface has been reported to form a continuous and homogeneous oxide layer without spallation [11], which is expected to benefit the wear resistance.

The HIP process at 1250°C kept the texture unchanged, only slightly improving the texture strength (Fig. 3), which might relate to the

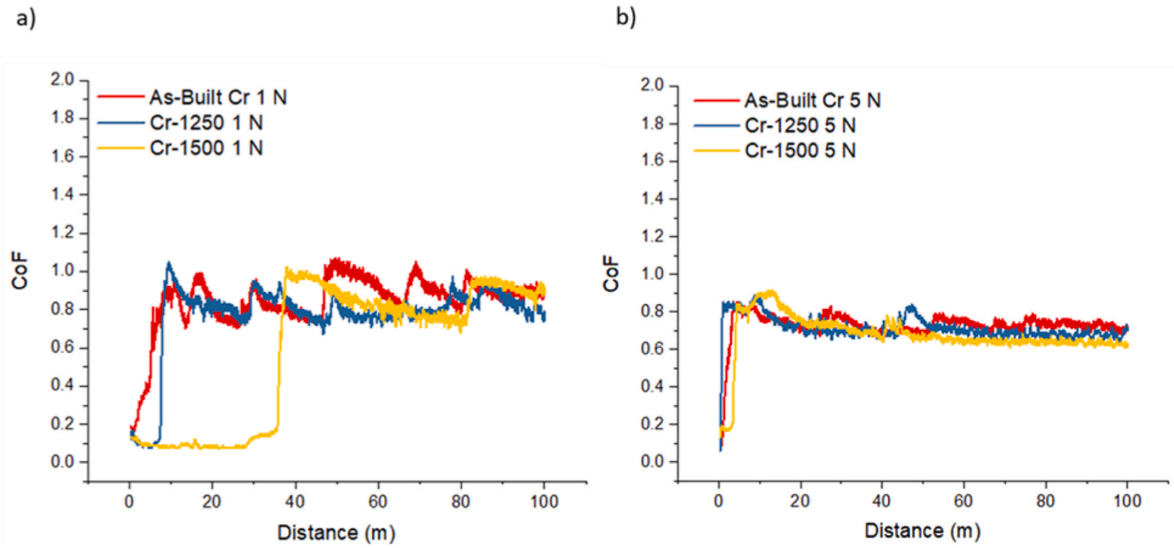

Fig. 7. CoF values of as-built and HIPed Cr samples under a) 1 N and b) 5 N loading conditions.

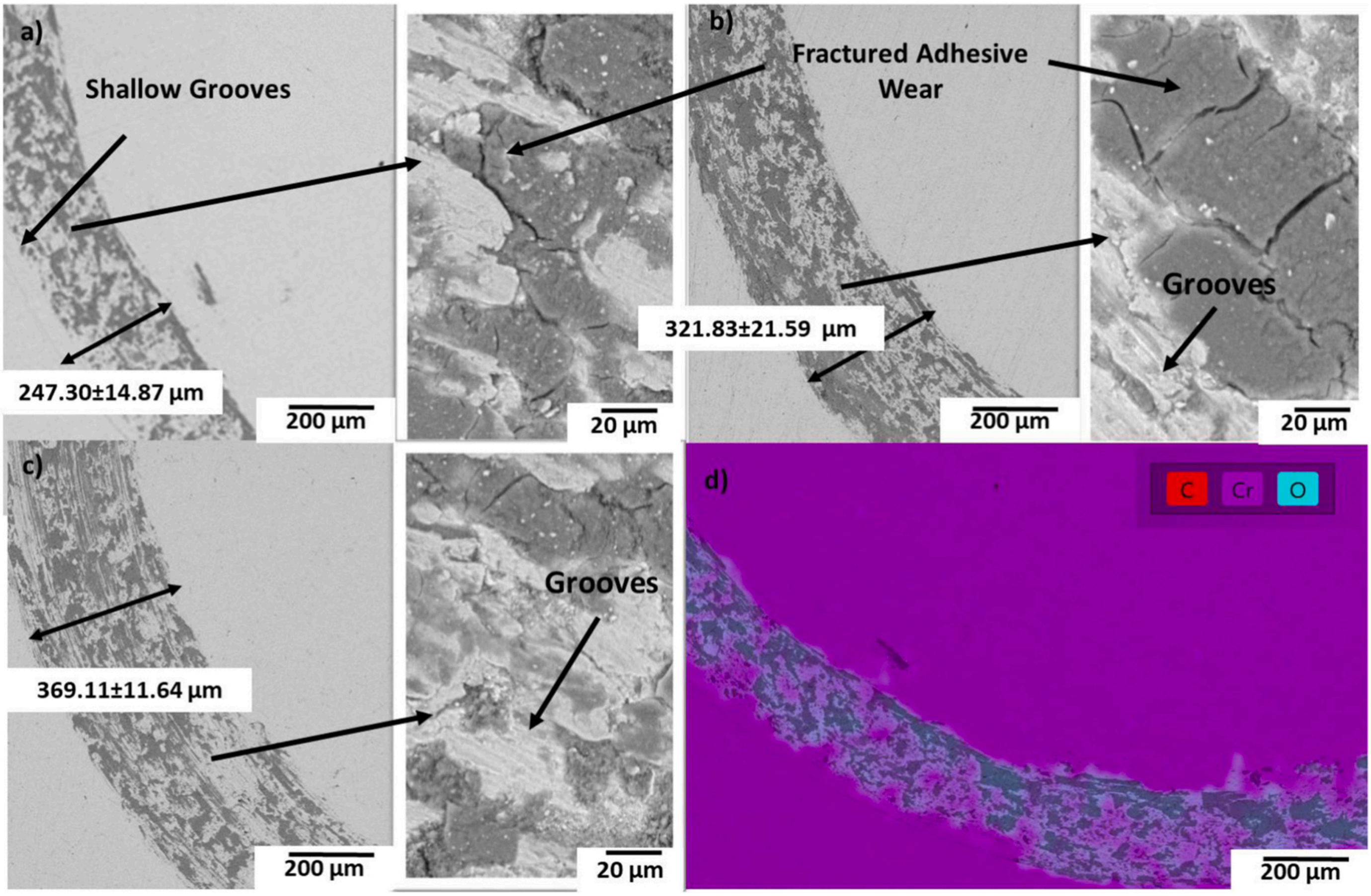

Fig. 8. Wear Tracks obtained under 1 N load for a) as-built, HIPed at b) 1250°C and c) 1500°C temperatures with d) EDS mapping image of as-built Cr sample.

recovery of misorientation in the grain and decrease in residual stress (Fig. 5), which are recovery structures [36]. Moreover, Cr-1250 exhibited 17% grain growth (Fig. 4) and consequently decrease in HAGB density.

On the other hand, the HIP process at 1500°C resulted in significant recrystallization, causing 2.5 times the grain size of the as-built Cr. Moreover, the columnar grain characteristics of as-built Cr changed to a larger equiaxed grain structure as identified in Fig. 3 owing to high HIP temperature promoting recrystallization and grain growth (Fig. 6) and thus promising isotropic characteristic.

This alteration in grain structure indicated that the HIP process at 1250°C was not sufficient to establish recrystallization and grain growth; rather, it resulted in partial defect annihilation and rearrangement of grain misorientation, showing the decrease in residual stress and

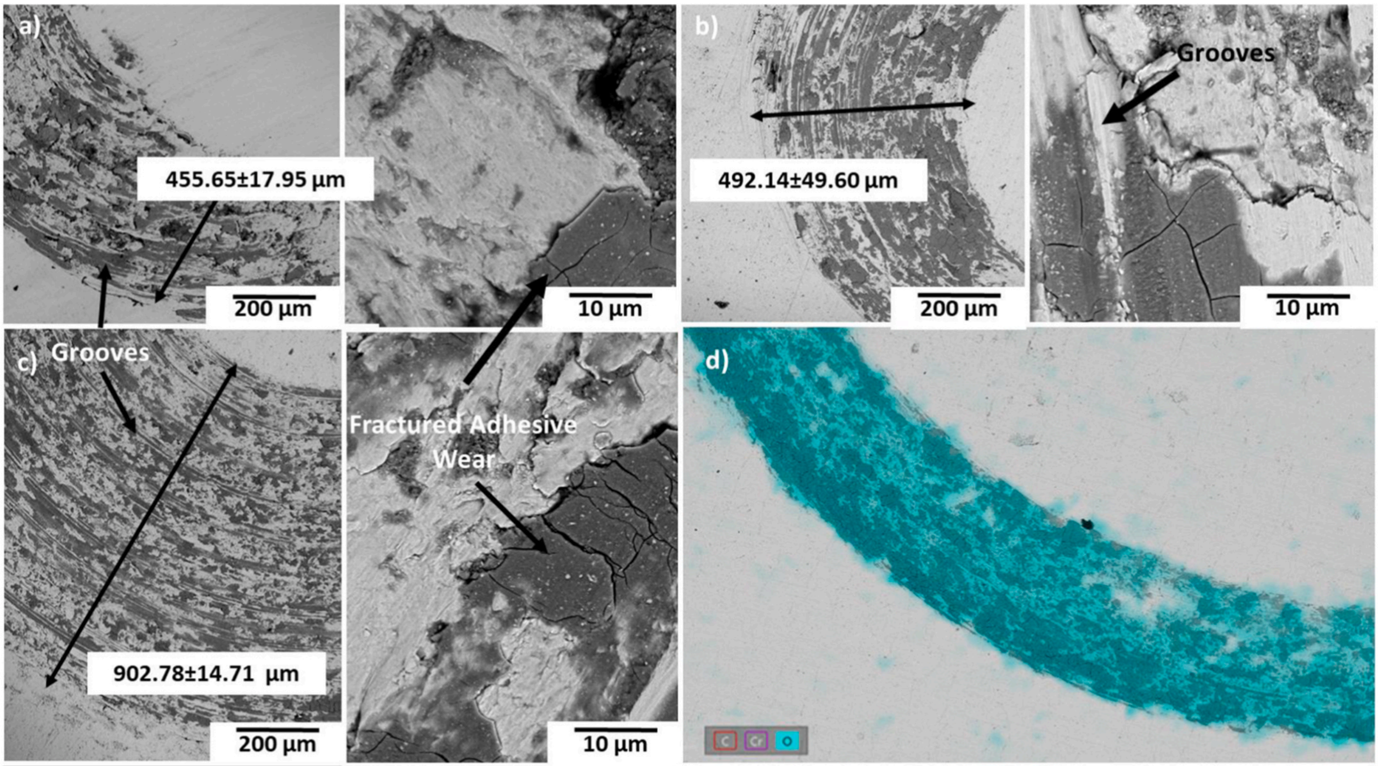

Fig. 9. Wear Tracks obtained under 5 N load for a) as-built, HIPed at b) 1250°C and c) 1500°C temperatures with d) EDS mapping image of as-built Cr sample.

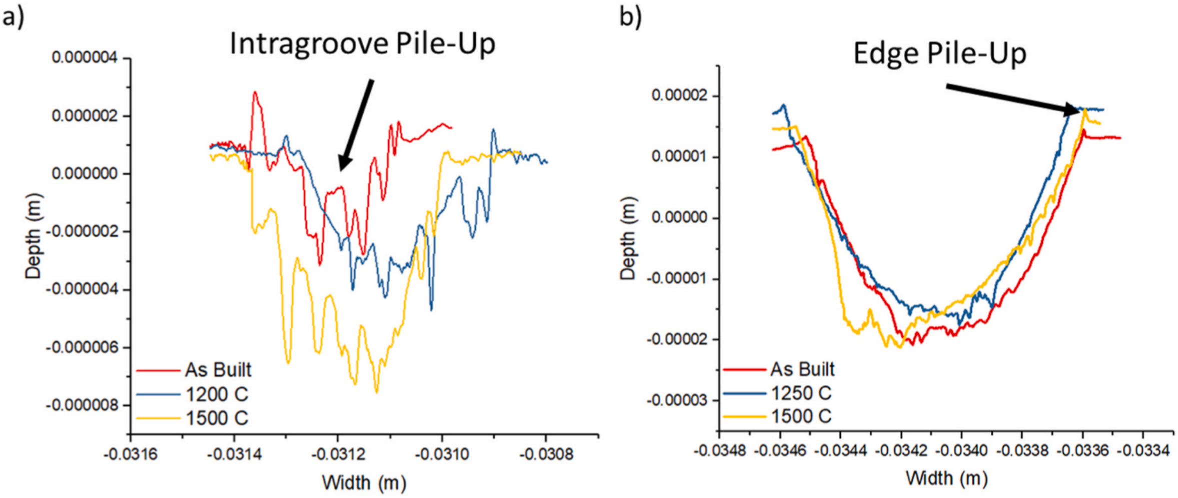

Fig. 10. 2D wear track debris for as-built and HIPed Cr: a) 1 N loading condition b) 5 N loading condition.

the ratio of deformed grains. However, the HIP process at 1500°C demonstrated complete stress relief and over 90% recrystallized grain characteristics, indicating that the 1500°C process temperature was efficient in activating full recrystallization and grain growth, allowing crack healing through absorption and assimilation of defects into growing grains, thus enhancing densification. More importantly, the Cr-1500 sample exhibited texture strengthening owing to recrystallization and <100> preferential growth direction, reaching the highest MUD value of 5.6, indicating homogeneous and stable oxide layer formation [11], which is significant for wear performance. Considering the altered texture strength, comparing as-built with HIPed Cr samples, the effect of the difference in texture strength on oxide layer characteristics should be further investigated in a future study.

In this regard, it is important to note that the high HIP temperature can demolish the microstructural anisotropy caused by the LPBF process. However, microstructure characteristics unique to LPBF, such as grain orientation via epitaxial growth and high residual stress (indicating high dislocation–deformed grains), which increase the hardness of the component, are beneficial for tribological performance.

It is well-established that the hardness of the sample correlates with its wear performance, of which the cracks in the samples mitigate the mechanical strength of the material. Therefore, the HIP temperature should be carefully determined to enhance the density rather than altering the beneficial microstructural features. Thus, according to the findings of this study, it is recommended to reach the highest possible density by optimizing the LPBF process parameter [28,29] and performing HIP at a medium temperature range to keep the advantageous microstructural features of LPBF processing. Otherwise, it is important

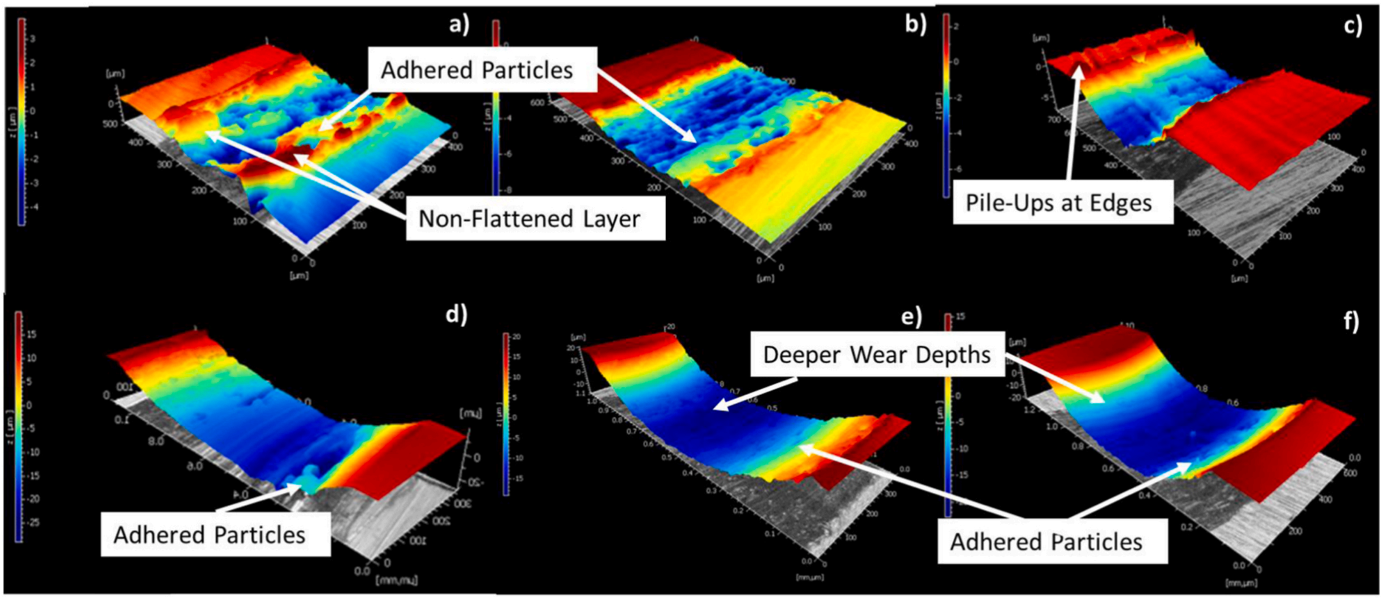

Fig. 11. 3D optical profilometer results under 1 N load for a) as-built, HIPed at b) 1250°C and c) 1500°C temperatures, 5 N load for d) as-built, HIPed at e) 1250°C and f) 1500°C.

for future studies focusing on LPBF processing of refractory metals and alloys to implement trace element addition [37], grain refinement [38], oxide and\or carbide nanoparticle inoculation [39] or in-situ nano-precipitate formation [40] to enhance the ductility and to prevent excessive grain growth during HIP process via Zener pinning effect [41] to accommodate advantages of both LPBF- and HIP-induced microstructural features.

4.2. The effect of HIP temperature on tribological behavior

From the findings of this study, it can be deduced that the initial and progressive stages of the wear test suggested different tribological behavior affected by various material properties such as materials' mechanical properties [42,43], surface condition [44], and the existence of lubricant phases such as oxides [45].

The CoF variations for the two different loads (1 N and 5 N) and the three sample conditions varied in running-in and steady-state stages in this study. For the 1 N load (Fig. 7a), the running-in stage is clearly observed with high deviations. As-built sample quickly reached higher CoF values, while Cr-1250 and Cr-1500 samples maintained CoF around 0.1, thus the lowest CoF observed. The oxide layer provides a lubricating effect that initially performs lower CoF under low applied loads [46–48]. The detectable delay and sudden increase of CoF were observed, especially under 1 N load for Cr-1250 and Cr-1500 samples, point wear acceleration or even failure with the damage of oxide layer [49], suggesting that the highly textured Cr-1500 formed a wear-resistant oxide layer which differed in CoF at the running-in stage. Such a significant increase in CoF has been reported in previous studies [49,50]. After the 8 m and 28 m distances of the test, the Cr-1250 and Cr-1500 sample surface oxide layers exhibited localized oxide disruptions. These disruptions led to the detachment of hard oxide particles from the surface, which activated a three-body abrasive wear mechanism. In this mechanism, the detached hard oxide particles become trapped between sliding contact surfaces, contributing to high CoF deviations under the 1 N loading condition. As a result, a steady-state stage is not evident under 1 N loading, as the CoF fluctuates significantly throughout the test for a 100 m testing length.

Under 1 N loading condition, oxide layer damage wear was common as seen in SEM images, Fig. 8, fractured adhesive wear. Under these adhered particles, grooves were visible due to the microploughing. Furthermore, 3D profilometric analyses of the wear tracks (Fig. 10) also confirmed these findings by revealing grooves, pile-up even in the inner parts of wear tracks, and increased particle accumulation, particularly in the Cr-1500 sample. Under 1 N, the as-built surface showed the shallowest and narrowest scar, while HIP at 1250°C produced wider tracks with partial edge ridges. The Cr-1500 sample already exhibited pronounced edge deformation even at this lower load. The wear width increased with increased HIP temperature, which indicated the negative effect of existing cracks, decreased hardness, and grain coarsening [51].

However, the increased wear load from 1 N to 5 N did not cause a linear increase in wear damage, indicating that the surface under the load was strengthened through strain hardening. Therefore, under 5 N loading (Fig. 7b), a more defined steady-state region emerges after the running-in stage. A higher load promoted more stable frictional behavior and steady-state performance as seen in Fig. 7b. Moreover, the lubricating effect of the oxide layer at higher load was observed in the Cr-1500 sample, similar to 1 N load. In the author's previous report [11] (100)-textured Cr samples exhibited a homogeneous and continuous oxide layer compared to randomly textured ones. This was reflected in the CoF graph as lower values at the initial sliding distances, particularly under the 1 N loading and even higher load condition. In the present study, the increase in HIP temperature led to higher MUD values, indicating a grain reorientation toward <100> easy growth direction. This reorientation was expected to promote the formation of a homogeneous oxide layer that provided initial wear resistance under various loading conditions, despite being mechanically unstable and prone to fragmentation under continued wear exposure. In the case of the steady-state stage, the mechanical response of the Cr sample regarding its microstructural characteristics was significant in determining its wear performance.

In the Cr-1500 sample, owing to the temperature-induced grain growth, the crack density was lower than that of other samples, reaching the highest density observed in this study. This result likely contributed to fluctuations in the CoF during sliding, potentially associated with detached wear debris from the surface[51–53].

Under 5 N loading conditions, plastic wear deformation increased in all samples but especially for Cr-1500, wider grooves are visibly different than 1 N loading conditions, which point to the dominant plastic and three-body deformation wear mechanisms. For the 1 N loading condition, in the CoF graph more pronounced deviations were observed for all samples (Fig. 7a). Under the 5 N loading condition, these deviations were decreased due to the higher contact stresses. Especially for Cr-1500 sample, after reaching the stable period of sliding distance (approximately 50 m), the lowest CoF value was observed compared to the other samples (Fig. 7b). However, this did not correspond to an overall improvement in tribological performance, which remained constrained by increased wear damage. As seen in Fig. 9c, the re-adhered particles were smeared and fractured again due to the heavier loading, which points to a fatigue wear mechanism.

By increasing the HIP temperature, defect reduction was achieved, leading to an increase in density, which was also emphasized regarding the changes in microstructural features. The potential positive effect of this was observed at low wear loads, where CoF values remained relatively low at the early stage, and wear track widths were comparable after 100 m of wear performance. However, the adverse effects of high HIP temperatures on grain size, microstructure, and hardness were particularly pronounced under a 5 N load, significantly deteriorating wear performance, while the as-built condition performed better owing to microstructure characteristics, such as small grain size and high residual stress, thus enhancing its hardness, which is a critical value discussing the wear performance. In the optical profilometer investigation, the differences became more distinct: the as-built sample maintained relatively moderate grooves, whereas HIP-1250°C revealed deeper pits and stronger edge flow. The HIP-1500 sample showed the most severe damage with the broadest, deepest wear scar in agreement with the highest wear volumes reported in Table 4, while the SEM (Fig. 9) observations support these results by revealing surface disruptions that consistent with material removal.

In the central regions, this reduction in porosity is fully consistent with the fundamental densification mechanism of HIP and is an expected outcome [54–56]. However, the increase in defects observed in the top and side regions can be explained by known limitations, such as the risk of near-surface pores opening up during HIP besides the expansion of trapped gases under high temperature and pressure can counter the effect of external pressure for the internal defects/cracks while resulting in stress redistribution during cooling. As highlighted previously, there are still limitations of the HIP process because of its limited diffusion, the negative effect of trapped internal protective gases, and the size of pores-defects [55,57,58]. A previous study [31] also showed that the densification of Ti6Al4V is complicated by near-surface pores. These pores were found to pose varying degrees of problems, sometimes even perforating the surface to create new external notches. These contradictory effects were particularly pronounced under a 5 N load, where the adverse effects of high HIP temperatures on grain size, microstructure, and hardness significantly deteriorated wear performance. In contrast, the as-built condition performed better owing to microstructural characteristics such as small grain size and high residual stress, which enhanced its hardness as a critical parameter in discussing wear behavior.

While this study provided insight into the effect of HIP temperature on defect prevention and enhanced densification of refractory metals and alloys, implementation of preheat, powder characteristics, and scan length can be proposed to decrease the defects prior to the HIP process as our previous studies highlighted the effectiveness of these approaches to enhance heat accumulation during the LPBF process, resulting in densification. [29,59]. Furthermore, the implementation of an optimized HIP process, considering the process temperature and pressure, can be proposed to eliminate cracks, particularly in the central region of refractory metals and alloys. In the aspect of post-processing application to improve component properties, moderate HIP temperature (1250°C) promotes recovery and partial stress relief but may induce surface crack propagation, while high HIP temperature (1500°C) enables recrystallization, grain growth, and crack healing, significantly increasing density. The transition from fine, high-stress microstructure to coarse, recrystallized grains reduces hardness but enhances oxide layer stability due to <100> texture development. This leads to a trade-off between mechanical strength and tribological performance, where high hardness governs wear resistance at low HIP temperatures, while oxide-assisted lubrication influences friction behavior at high HIP temperatures.

5. Conclusion

The effect of HIP treatment and applied temperature on LPBF-processed pure Cr samples' microstructure and tribological performance was investigated in this study. Based on the results obtained in this study, the following conclusion can be drawn:

1. HIP processing reduced internal cracks in the center region of pure refractory Cr fabricated by the LPBF process.
2. 1250°C HIP processing temperature (T/T_m (K) > 0.5) slightly affected grain characteristics, increasing the fraction of substructure grain. The ratio of deformed grains decreased with partial recovery.
3. At 1500°C HIP application (T/T_m (K) > 0.8), the highest density was achieved, although the cracks were not completely eliminated, particularly open-surface defects.
4. High-temperature HIP led to a reduction in high-angle grain boundaries and further decreased the fraction of deformed grains. Significant grain growth\ recrystallization resulted in the formation of equiaxed grains. Although grain growth resulted in lower hardness, Cr-1500 samples showed highest <100> grain orientation, indicating improved oxidation properties.
5. In terms of wear mechanism, all samples showed abrasive and adhesive wear, leading to high friction coefficient values and deviations under 1 N loading. However, as-built Cr with the highest hardness exhibited smallest wear track width and wear volume owing to fine microstructure, high residual stresses, and a greater proportion of deformed grains.
6. Cr-1500 samples reaching the highest density formed a protective oxide layer owing to strong <100> grain orientation as observed with the delay in CoF up to 40 m under 1 N load.
7. After a certain number of cycles, damaged oxide layer caused wear acceleration in all samples, resulting in a three-body abrasive wear mechanism and a significant increase in CoF, which evidently observed with HIPed Cr samples.

Further research on this topic requires consideration of oxide\carbide nanoparticle inoculation to prevent grain growth during HIP process at high temperatures by Zener pinning effect on the grain boundaries while providing oxide disperse strengthening. By this approach, it is possible to utilize advantages of both LPBF and HIP processes for structural applications of refractory metals and alloys.

Author contributions: CRediT

Ozkan Gokcekaya: Conceptualization, Methodology, Investigation, Formal analysis, Data curation, Funding acquisition, Writing – original draft, Writing – review & editing.

Asli Gunay Bulutsuz: Conceptualization, Methodology, Investigation, Formal analysis, Data curation, Writing – original draft, Writing – review & editing.

Buse Gulec: Formal analysis, Investigation.

Ali Gunen: Methodology, Writing – review & editing.

Hakan Yilmazer: Conceptualization, Writing – review & editing.

Takayoshi Nakano: Supervision, Funding acquisition, Writing – review & editing.

Declaration of competing interest

The authors declare that they have no known competing financial interests or personal relationships that could have appeared to influence the work reported in this paper.

Acknowledgement

This work was supported by a Grant-in-Aid for Scientific Research (JP24K07254) from the Japan Society for the Promotion of Science (JSPS) and CREST-Nanomechanics: Elucidation of macroscale mechanical properties based on understanding the nanoscale dynamics of innovative mechanical materials (Grant Number: JPMJCR2194) from the Japan Science and Technology Agency and the Scientific and Technological Research Council of Turkey (TUBITAK) BIDEB 2209-A (Grant Number: 1919B012102207).

References

[1] Provenzano V, Krasilnikov NA, V Pavlenko D, Rickerby DG, Zhilyaev AP. In: Lowe TC, Valiev RZ, editors. Structure and mechanical properties of ultrafine-grained chromium produced by severe plastic deformation processing BT - investigations and applications of severe plastic deformation. Dordrecht: Springer Netherlands; 2000. p. 281–7. https://doi.org/10.1007/978-94-011-4062-1_36.

[2] Schuster BE, Ligda JP, Pan ZL, Wei Q. Nanocrystalline refractory metals for extreme condition applications. JOM 2011;63:27–31. https://doi.org/10.1007/s11837-011-0202-3.

[3] Ury N, Ravi V. The effects of chromium on the high temperature corrosion of Ni–Cr alloys exposed to calcium sulfate, high temp. Corros Mater 2024;101:603–20. https://doi.org/10.1007/s11085-024-10232-3.

[4] Isshiki M, Arakawa K, Igaki K, Mizohata A, Tsujimoto T. Preparation of high purity chromium. J Less Common Met 1984;96:157–63. https://doi.org/10.1016/0022-5088(84)90190-5.

[5] Briant CL, Kumar KS, Rosenberg N, Tomioka H. The mechanical properties of high purity chromium. Int J Refract Met Hard Mater 2000;18:9–11. https://doi.org/10.1016/S0263-4368(99)00031-1.

[6] Bahrami A, Delgado A, Onofre C, Muhl S, Rodil SE. Structure, mechanical properties and corrosion resistance of amorphous Ti-Cr-O coatings. Surf Coatings Technol 2019;374:690–9. https://doi.org/10.1016/j.surfcoat.2019.06.061.

[7] Dorcheh AS, Galetz MC. Challenges in developing oxidation-resistant chromium-based alloys for applications above 900°C. JOM 2016;68:2793–802. https://doi.org/10.1007/s11837-016-2079-7.

[8] Issa I, Hohenwarter A, Fritz R, Kiener D. Fracture properties of ultrafine grain chromium correlated to single dislocation processes at room temperature. J Mater Res 2019;34:2370–83. https://doi.org/10.1557/jmr.2019.140.

[9] Holzwarth U, Stamm H. Mechanical and thermomechanical properties of commercially pure chromium and chromium alloys. J Nucl Mater 2002;300:161–77. https://doi.org/10.1016/S0022-3115(01)00745-0.

[10] Gu YF, Harada H, Ro Y. Chromium and chromium-based alloys: problems and possibilities for high-temperature service. JOM 2004;56:28–33. https://doi.org/10.1007/s11837-004-0197-0.

[11] Gokcekaya O, Hayashi N, Ishimoto T, Ueda K, Narushima T, Nakano T. Crystallographic orientation control of pure chromium via laser powder-bed fusion and improved high temperature oxidation resistance. Addit Manuf the publication year 2020 2020;36:101624. https://doi.org/10.1016/j.addma.2020.101624.

[12] DebRoy T, Wei HL, Zuback JS, Mukherjee T, Elmer JW, Milewski JO, Beese AM, Wilson-Heid A, De A, Zhang W. Additive manufacturing of metallic components – process, structure and properties. Prog Mater Sci 2018;92:112–224. https://doi.org/10.1016/j.pmatsci.2017.10.001.

[13] Köhler ML, Radtke F, Norda M, Herzog S, Kaletsch A, Petzoldt F, Broeckmann C. Resistance against abrasive wear and corrosion of laser powder bed alloyed high chromium tool steels. Steel Res Int 2023;94:2200455. https://doi.org/10.1002/srin.202200455.

[14] Bera T, Mohanty S. A review on residual stress in metal additive manufacturing, 3D print. Addit Manuf 2023;11:1462–70. https://doi.org/10.1089/3dp.2023.0095.

[15] Herzog D, Seyda V, Wycisk E, Emmelmann C. Additive manufacturing of metals. Acta Mater 2016;117:371–92. https://doi.org/10.1016/j.actamat.2016.07.019.

[16] Lv Z, Lu M, Xiao G, Ma Y, Weng D, Wang B, Shang Z, Qi W, Chen L, Chang J, Wang J. A review of near-net shape forming by hot isostatic pressure technology. J Am Ceram Soc 2025;108:e20196. https://doi.org/10.1111/jace.20196.

[17] Ng CH, Bermingham MJ, Dargusch MS. Eliminating porosity defects, promoting equiaxed grains and improving the mechanical properties of additively manufactured Ti-22V-4Al with super-transus hot isostatic pressing. Addit Manuf 2023;72:103630. https://doi.org/10.1016/j.addma.2023.103630.

[18] Wang K, Liu W, Li X, Tong Y, Hu Y, Hu H, Chang B, Ju J. Effect of hot isostatic pressing on microstructure and properties of high chromium K648 superalloy manufacturing by extreme high-speed laser metal deposition. J Mater Res Technol 2024;28:3951–9. https://doi.org/10.1016/j.jmrt.2023.12.280.

[19] Kim Y-K, Yoon T-S, Lee K-A. Effect of hot isostatic pressing on the microstructure and room·high temperature tensile properties of fe-cr-ni based HK30 alloy manufactured by metal injection molding process. Korean J Met Mater 2018;56:121–9. https://doi.org/10.3365/KJMM.2018.56.2.121.

[20] Grech IS, Sullivan JH, Lancaster RJ, Plummer J, Lavery NP. The optimisation of hot isostatic pressing treatments for enhanced mechanical and corrosion performance of stainless steel 316L produced by laser powder bed fusion. Addit Manuf 2022;58:103072. https://doi.org/10.1016/j.addma.2022.103072.

[21] Mishurova T, Evsevleev S, Piault P, King A, Henry L, Bruno G. Understanding the hot isostatic pressing effectiveness of laser powder bed fusion Ti-6Al-4V by in-situ X-ray imaging and diffraction experiments. Sci Rep 2023;13:18433. https://doi.org/10.1038/s41598-023-45258-1.

[22] Kunz J, Boontanom A, Herzog S, Suwanpinij P, Kaletsch A, Broeckmann C. Influence of hot isostatic pressing post-treatment on the microstructure and mechanical behavior of standard and super duplex stainless steel produced by laser powder bed fusion. Mater Sci Eng A 2020;794:139806. https://doi.org/10.1016/j.msea.2020.139806.

[23] Aghayar Y, Shahriari A, Moazzen P, Mohammadi M. Hot isostatic pressing of additively manufactured metallic components: a critical review on microstructure, mechanical, and corrosion properties. J Mater Res Technol 2026;40:3343–81. https://doi.org/10.1016/j.jmrt.2025.12.306.

[24] Bahshwan M, Myant CW, Reddyhoff T, Pham M-S. The role of microstructure on wear mechanisms and anisotropy of additively manufactured 316L stainless steel in dry sliding. Mater Des 2020;196:109076. https://doi.org/10.1016/j.matdes.2020.109076.

[25] Aghayar Y, Shahriari A, Shakerian M, Purdy M, Mohammadi M. Microstructure tailoring of laser powder bed fused 316L impellers for enhanced mechanical properties and optimum electrochemical characteristics through hot isostatic pressing. Mater Sci Eng A 2025;925:147916. https://doi.org/10.1016/j.msea.2025.147916.

[26] Aghayar Y, Behvar A, Antu MNR, Avateffazeli M, Haghshenas M, Mohammadi M. Ambient and high-temperature rotating bending fatigue of as-built and hot isostatic pressed additively manufactured 316L stainless steel. Int J Fatig 2026;204:109365. https://doi.org/10.1016/j.ijfatigue.2025.109365.

[27] Bulutsuz AG, Gulec B, Gokcekaya O, Gardstam J, Nakano T, Yilmazer H. An investigation over microstructure and HIP processing effects on wear performance of pure chromium parts fabricated by laser powder bed fusion. Int J Refract Met Hard Mater 2024;120:106616. https://doi.org/10.1016/j.ijrmhm.2024.106616.

[28] Kim YS, Gokcekaya O, Matsugaki A, Nakano T. Effect of laser scan speed on defects and texture development of pure chromium metal fabricated via powder bed fusion-laser beam. Materials 2024;17. https://doi.org/10.3390/ma17092097.

[29] Park S-H, Gokcekaya O, Nitomakida T, Nakano T. Effects of heat accumulation strategies on defects and microstructure of pure chromium fabricated by laser powder bed fusion: an experimental and numerical study. J Mater Res Technol 2024;33:7333–44. https://doi.org/10.1016/j.jmrt.2024.11.049.

[30] Nagase T, Hori T, Todai M, Sun S-H, Nakano T. Additive manufacturing of dense components in beta-titanium alloys with crystallographic texture from a mixture of pure metallic element powders. Mater Des 2019;173:107771. https://doi.org/10.1016/j.matdes.2019.107771.

[31] du Plessis A, Macdonald E. Hot isostatic pressing in metal additive manufacturing: X-ray tomography reveals details of pore closure. Addit Manuf 2020;34:101191. https://doi.org/10.1016/j.addma.2020.101191.

[32] Xin R, Ma Q, Li W. Microstructure and mechanical properties of internal crack healing in a low carbon steel. Mater Sci Eng A 2016;662:65–71. https://doi.org/10.1016/j.msea.2016.03.045.

[33] Wei D, Zhou W, Kong D, Tian Y, He J, Wang R, Huang W, Tan Q, Zhu G, Sun B. Pre-softening HIP treatment enabled crack-healing and superior mechanical properties for René 142 superalloy fabricated via laser powder bed fusion. J Mater Sci Technol 2025;210:58–71. https://doi.org/10.1016/j.jmst.2024.05.042.

[34] Li S, Lan X, Wang Z, Mei S. Microstructure and mechanical properties of Ti-6.5Al-2Zr-Mo-V alloy processed by Laser Powder Bed fusion and subsequent heat treatments. Addit Manuf 2021;48:102382. https://doi.org/10.1016/j.addma.2021.102382.

[35] Hooper PA. Melt pool temperature and cooling rates in laser powder bed fusion. Addit Manuf 2018;22:548–59. https://doi.org/10.1016/j.addma.2018.05.032.

[36] Zheng C, Wang Y, Jin J, Gong P, Wang X, Wen H, Zhang M. Recrystallization and grain growth behavior of variously deformed CoCrFeMnNi high-entropy alloys: microstructure characterization and modeling. J Mater Res Technol 2022;20:2277–92. https://doi.org/10.1016/j.jmrt.2022.07.182.

[37] Wang Y, Guo W, Li H, Cui H, Han P, Zhao D, Li S, Li Y, Huang S, Zhang H. High-temperature plasticity improvement by La addition during crack inhibition in laser powder bed fusion fabricated Haynes 230. Virtual Phys Prototyp 2025;20:e2504079. https://doi.org/10.1080/17452759.2025.2504079.

[38] Wang Y, Guo W, Liang X, Du B, Li H, Xu M, Zhang H, Lin F. Regulation of high-temperature oxidation behavior and crack inhibition mechanism in haynes 230 alloy fabricated by laser powder bed fusion. J Mater Res Technol 2026;42:3005–21. https://doi.org/10.1016/j.jmrt.2026.03.227.

[39] Funch CV, Proust G. Laser-based additive manufacturing of refractory metals and their alloys: a review. Addit Manuf 2024;94:104464. https://doi.org/10.1016/j.addma.2024.104464.

[40] Wang Y, Guo W, Li H, Xie Y, Shi J, Liang Z, Han P, Li S, Zhang H. Nano-scale microstructural evolution and mechanical property enhancement mechanism during crack inhibition in nickel-based superalloys fabricated by laser powder bed fusion. Addit Manuf 2025;100:104685. https://doi.org/10.1016/j.addma.2025.104685.

[41] Zhao X, Olden D, Williams B, Pariyar A, Zhang D, Murphy M, Reed P, Allison P, Jordon B, Qi J, Rainforth WM, Guan D. Grain growth stagnation at 525 °C by nanoparticles in a solid-state additively manufactured Mg-4Y-3RE alloy. J Magnes Alloy 2024;12:4976–87. https://doi.org/10.1016/j.jma.2024.12.010.

[42] Bulutsuz AG, Yurci ME, Ozaltin K, Chrominski W, Lewandowska M. Tribological behavior of a hydrostatically extruded ultra-fine grained Ti-13Nb-13Zr alloy, vol. 61; 2019. p. 543–8. https://doi.org/10.3139/120.111352.

[43] Günay Bulutsuz A. Tribological behavior of high-pressure torsion processed biodegradable pure Zn under dry and wet conditions. Ind Lubr Tribol 2022;74:542–9. https://doi.org/10.1108/ILT-09-2021-0366.

[44] Günen A, Kanca E, Karakaş MS, Koç V, Gök MS, Kanca Y, Çürük A, Demir M. High temperature wear behavior of the surface-modified externally cooled rolls. Surf Coatings Technol 2018;348:130–41. https://doi.org/10.1016/j.surfcoat.2018.04.071.

[45] Ahn H-S, Kwon O-K. Tribological behaviour of plasma-sprayed chromium oxide coating. Wear 1999;225–229:814–24. https://doi.org/10.1016/S0043-1648(98)00390-1.

[46] Wang Y, Liu X-B, Liu Y-F, Luo Y-S, Meng Y. Microstructure and tribological performance of Ni60-based composite coatings on Ti6Al4V alloy with different Ti3SiC2 ceramic additions by laser cladding. Ceram Int 2020;46:28996–9010. https://doi.org/10.1016/j.ceramint.2020.08.071.

[47] Cornacchia G, Cecchel S, Battini D, Petrogalli C, Avanzini A. Microstructural, mechanical, and tribological characterization of selective laser melted CoCrMo alloy under different heat treatment conditions and hot isostatic pressing. Adv Eng Mater 2022;24:2100928. https://doi.org/10.1002/adem.202100928.

[48] Tong Y, Zhang T, Zhang S. Influence of oxides on the formation of self-lubricating layer and anti-wear performance during sliding. Tribol Int 2023;179:108188. https://doi.org/10.1016/j.triboint.2022.108188.

[49] Li N, Li G, Wang H, Kang J, Dong T, Wang H. Influence of TiO2 content on the mechanical and tribological properties of Cr2O3-based coating. Mater Des 2015;88:906–14. https://doi.org/10.1016/j.matdes.2015.09.085.

[50] Cetinel H, Celik E, Kusoglu MI. Tribological behavior of Cr2O3 coatings as bearing materials. J Mater Process Technol 2008;196:259–65. https://doi.org/10.1016/j.jmatprotec.2007.05.048.

[51] AlMangour B, Grzesiak D, Yang J-M. Selective laser melting of TiB2/316L stainless steel composites: the roles of powder preparation and hot isostatic pressing post-treatment. Powder Technol 2017;309:37–48. https://doi.org/10.1016/j.powtec.2016.12.073.

[52] Hsia F-C, Elam FM, Bonn D, Weber B, Franklin SE. Wear particle dynamics drive the difference between repeated and non-repeated reciprocated sliding. Tribol Int 2020;142:105983. https://doi.org/10.1016/j.triboint.2019.105983.

[53] Mekicha MA, de Rooij MB, Mishra T, Matthews DTA, Jacobs L, Schipper DJ. Study of wear particles formation at single asperity contact: an experimental and numerical approach. Wear 2021;470–471:203644. https://doi.org/10.1016/j.wear.2021.203644.

[54] Sun S, Teng Q, Xie Y, Liu T, Ma R, Bai J, Cai C, Wei Q. Two-step heat treatment for laser powder bed fusion of a nickel-based superalloy with simultaneously enhanced tensile strength and ductility. Addit Manuf 2021;46:102168. https://doi.org/10.1016/j.addma.2021.102168.

[55] Nayak SK, Jinoop AN, Paul CP, Kumar VA, Subburaj D, Singh R, Bindra KS. On the hot isostatic pressing of inconel 625 structures built using laser powder bed fusion at higher layer thickness. Int J Adv Manuf Technol 2022;120:4065–78. https://doi.org/10.1007/s00170-022-08960-4.

[56] du Plessis A, Razavi N, Wan D, Berto F, Imdaadulah A, Beamer C, Shipley J, MacDonald E. Fatigue performance of shelled additively manufactured parts subjected to hot isostatic pressing. Addit Manuf 2022;51:102607. https://doi.org/10.1016/j.addma.2022.102607.

[57] Xu J, Ma T, Peng RL, Hosseini S. Effect of post-processes on the microstructure and mechanical properties of laser powder bed fused IN718 superalloy. Addit Manuf 2021;48:102416. https://doi.org/10.1016/j.addma.2021.102416.

[58] Mao J, Wu Z, Ye N, Wen X, Zhang F, Zhu W, Gong Z, Tang J. Compressive performance and defects healing behavior of pure tungsten fabricated by LPBF coupled with subsequent hot isostatic pressing. Int J Refract Met Hard Mater 2025;129:107100. https://doi.org/10.1016/j.ijrmhm.2025.107100.

[59] Gokcekaya O, Ishimoto T, Todo T, Wang P, Nakano T. Influence of powder characteristics on densification via crystallographic texture formation: pure tungsten prepared by laser powder bed fusion. Addit Manuf Lett 2021;1:100016. https://doi.org/10.1016/j.addlet.2021.100016.